Highly Efficient Solid-State Near-Infrared Emitting Material Based on Triphenylamine and Diphenylfumaronitrile with an EQE of 2.58% in Nondoped Organic Light-Emitting Diode

Xiao Han, Qing Bai, Liang Yao, Haichao Liu, Yu Gao, Jinyu Li, Liqun Liu, Yulong Liu, Xiaoxiao Li, Ping Lu, and Bing Yang*

The development of efficient near-infrared (NIR) emitting material is of current focus. Donor–acceptor (D–A) architecture has been proved to be an effective strategy to obtain narrow energy gap. Herein, a D–A-type NIR fluorescent compound 2,3-bis(4′-(diphenylamino)-[1,1′-biphenyl]-4-yl) fumaronitrile (TPATCN) is synthesized and fully characterized. As revealed by theoretical calculations and photophysical experiments, TPATCN exerts the advantages of the relatively large dipole moment of the charge transfer state and a certain degree of orbital overlap of the local excited state. A highly mixed or hybrid local and charge transfer excited state might occur to simultaneously achieve both a large fraction of singlet formation and a high quantum efficiency in D–A system. TPATCN exhibits strong NIR fluorescence with the corresponding thin film quantum efficiency of 33% and the crystal efficiency of 72%. Remarkably, the external quantum efficiency of nondoped NIR organic light-emitting diode (OLED) reaches 2.58% and remains fairly constant over a range of 100–300 mA cm^{-2}, which is among the best results for NIR OLEDs reported so far.

1. Introduction

With the rapid development of organic light-emitting diodes (OLEDs) in the past years, luminescent materials covering full RGB colors have made great progress in terms of luminance and efficiency.[1] Tuning the emission wavelength of OLEDs to the deep red and near-infrared (NIR) regions is of current focus due to their wide applications in night vision, telecommunications, and bioimaging.[2] Although some phosphorescent materials based on transition metal complexes, such as platinum (Pt) complexes, have already realized external quantum efficiency (EQE) over 9%,[3] they suffer heavily from sharp efficiency roll-off at high brightness. The metal-free organic materials are significantly important for the mass production in realistic point of view owing to their low cost, non-involving of poor reproducibility of the optimum doping level, and concise control in device fabrication required for metal-complexed phosphorescent materials.[4] In principle, red fluorescent emission comes from a narrow bandgap. To date, fluorophores with narrow bandgap either have extended π conjugation or possess polar donor–acceptor (D–A) architectures.[5] The latter one has been proved to be a very promising way to effectively extend the emission to long wavelength. In addition, D–A system is also beneficial to the recombination of carriers because the modification of low highest occupied molecular orbital (HOMO) and lowest unoccupied molecular orbital (LUMO) energy levels will effectively lower the injection barriers for electrons and holes in OLEDs.[6] More importantly, the electron flip can take place since the charge transfer (CT) excitons formed between the donor and acceptor is a weak Coulomb hole–electron pair, which would facilitate a large fraction of singlet excitons formation under electrical charge injection.[7] However, a major shortcoming of D–A compound is that the spatially separated HOMO–LUMO orbitals always result in the forbidden electronic transition, which usually leads to the low photoluminescence quantum efficiency.[1d,5] In contrast, the fluorophores with local excited (LE) states are generally reported to acquire high photoluminescence quantum efficiency; however, such fluorophores generally exhibit low singlet exciton yields originated from the forbidden spin flip from triplet state to singlet state and their electroluminescent internal quantum efficiencies are limited to ≈25%.[8] Recently, materials based on new principle, such as hybridized local and charge transfer (HLCT) with excitons that undergo a reverse intersystem crossing process (RISC) along the high-lying CT channel, has emerged to reach a compromise of LE and CT states to break through the 25% upper limit of η_s.[9] Unlike many D–A compounds suffering from the low efficiency originated from CT effects, these materials benefit from the large dipole moment of the CT state and a certain degree of orbital overlap of the LE state, which is a promising way to endow the material with a high photoluminescence quantum efficiency as well as a large singlet exciton yield.

Dr. H. Xiao, Q. Bai, Dr. L. Yao, Dr. H. Liu, Dr. Y. Gao, Dr. J. Li, L. Liu, Dr. Y. Liu. X. Li, Prof. P. Lu, Prof. B. Yang
State Key Laboratory of Supramolecular Structure and Materials
Jilin University
Changchun 130012, P. R. China
E-mail: lup@jlu.edu.cn

DOI: 10.1002/adfm.201503344

In order to construct a NIR molecule in a D–A system, relatively strong donor and acceptor units should be adopted to efficiently decrease the bandgap. In prior studies, several electron acceptors, such as dithienylbenzothiadiazole (BBT), benzo[1,2-*c*:4,5-*c*]bis([1,2,5]thiadiazole) (BBTD), and [1,2,5] thiadiazolo[3,4-*g*]quinoxaline (QTD), have become the workhorses in the development of red or NIR D–A materials.[10] However, most of these units usually showed low fluorescent in the solid state because the molecular aggregations are prone to cause the quenching of fluorescence. What is more, vibronic coupling between ground and excited states originated from their intrinsic relatively low bandgap would also increase the nonradiative pathways to further decrease the solid-state efficiency.[1b,10a,b] According to Equation (1), where η_r is the radiative exciton ratio, η_{ext} is

$$\eta_{ext} = \gamma \eta_r \eta_{out} \eta_{PL} \quad (1)$$

the external quantum efficiency, η_{out} is the light outcoupling efficiency, η_{PL} is the intrinsic photoluminescence efficiency, and γ is the recombination efficiency of injected holes and electrons; it can be anticipated that the efficient emission in solid state is one prerequisite to reach a high η_{ext}. For this purpose, diphenylfumaronitrile (DBFN) unit has drawn our attention because it is found to possess high solid-state efficiency and the two cyano functionalities allow for great electron delocalization to effectively reduce the bandgap. For example, in 2003, Chen and co-workers have pointed out that DBFN-cored derivative, NPAFN, was unusual because it was brightly fluorescent only in the solid state with red emission at 616 nm.[11] In 2013, Tang and co-workers have reported a DBFN-containing BTPEFN exhibited efficient orange fluorescence with a high quantum efficiency of nearly 100% in film.[12] However, the efficient NIR emission based on DBFN has not yet been realized. In this work, triphenylamine (TPA),[13] which contains sp^3 N atom with lone pair electron is selected as the relatively strong donor. Fusing these two units into one system via D–A–D linking fashion, two biphenyl structure which could rotate freely around the single bond will be generated, which endows multiple configuration of the molecule giving rise to the formation of suitable torsion angel between D–A groups and further facilitating the "hot exciton" process as demonstrated before.[9] Guided by this design principle, we report the D–A–D-type NIR fluorescent compound, TPATCN, with a strong NIR emission and a film efficiency of 33%. TPATCN is found to possess a high photoluminescence quantum efficiency as well as a large singlet exciton yield as anticipated. The maximum EQE of its nondoped device reaches 2.58% with good color stability, which is among the highest values of NIR OLEDs. The radiative exciton ratio is calculated to be 39%, which exceeds the upper limit η_s of 25%.

2. Results and Discussions

2.1. Synthesis and Characterization

The chemical structures of TPATCN are shown in Scheme S1 (Supporting Information). TPATCN was prepared according to a Suzuki coupling reaction between corresponding 2,3-bis(4-bromophenyl)fumaronitrile and *N*,*N*-diphenyl-4-(4,4,5,5-tetramethyl-1,3,2-dioxaborolan-2-yl)aniline with a high yield. TPATCN was fully by ^{1}H NMR, MS, FTIR, elemental analysis and corresponded well with its expected structure (see the Supporting Information). It shows good solubility in common organic solvents, such as toluene, tetrahydrofuran (THF), dichloromethane (DCM), chloroform, and ethyl acetate. Thermogravimetric analysis (TGA) was carried out under nitrogen atmosphere to investigate the thermal properties. TPATCN exhibited a very high decomposition temperature (T_d, corresponding to 5% weight loss) 495 °C, indicating its excellent thermal stability, which is an important factor to get appreciable device performance.

2.2. Theoretical Calculations

To understand the electronic properties of TPATCN, density functional theory (DFT) calculations were carried out with the ground state geometry optimized at the B3LYP/6-31G(d,p) level.[14] The distributions of the frontier molecular orbital at ground state are shown in **Figure 1**b. The HOMO of TPATCN was mainly located on the TPA unit with sizeable distribution on two central phenyl rings and olefin bond, whereas the LUMO level was mostly distributed on the central fumaronitrile core. Thus, the HOMO and LUMO distributions were well overlapped on newly formed two biphenyl π bridges and fumaronitrile unit, while fully separated on the terminal diphenylamine moiety. Although the relatively strong electron donor and acceptor units existed simultaneously, the insufficient separation of the HOMO and LUMO energy levels of TPATCN suggested its different characteristics from those materials with strong intramolecular CT, in which the completely separation of the HOMO and LUMO energy levels were usually observed.[5,15] The calculated HOMO and LUMO were −5.04 and −2.65 eV, respectively, resulting in the narrow bandgap of 2.39 eV. To further describe the excited state properties of TPATCN, we also calculated the natural transition orbital (NTO) of the singlet and triplet states to analyze electron transition characters (Figure 1c; Figures S7 and S8, Supporting Information). Observed from the lowest singlet state of S_1 (3.04 eV), the hole was distributed on the whole molecule skeleton and the particle was localized on the central fumaronitrile core. The overlap of hole and particle demonstrated the coexistence of CT and LE components which was proposed to be HLCT state. In a way, TPATCN might achieve high photoluminescence quantum yield (η_{PL}). Furthermore, TPATCN possessed special excited state energy level structures. The lowest triplet state, T_1 (2.23 eV), was an LE state with its hole and particle were both located on central fumaronitrile core, while the high-lying triplet excited state, T_2 (2.93 eV), was proposed to be HLCT state with configuration similar to the S_1. The large energy split (0.7 eV) between T_2 and T_1 suppressed internal conversion (IC) process from T_2 to T_1, and the small energy split (only 0.1 eV) between T_2 and S_1 facilitated the RISC process from T_2 to S_1 (Figure 1d). These NTOs characters of TPATCN were in consistent with "hot exciton" principle as reported before,[9] which was expected to be a promising way to obtain high exciton utilization (η_s) ratio over 25% in OLEDs. The special excited state

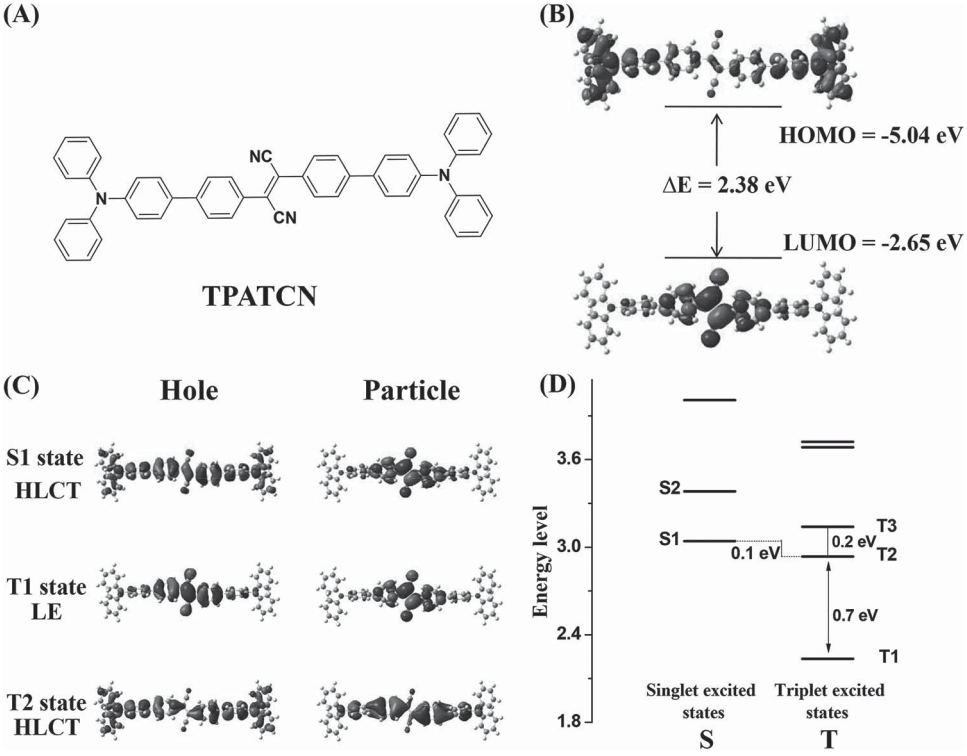

Figure 1. A) Molecular structure of TPATCN; B) HOMO and LUMO distribution of TPATCN at ground state; C) nature transition orbitals for S_1, T_1, and T_2; D) the energy landscape for singlet and triplet excited states.

energy level structures of TPATCN triggered us to study the energy level of central core DBFN in excited state, which had not been investigated in prior study. According to the calculation results of the energy landscape of the singlet and triplet states of DBFN (Figure S9, Supporting Information), the large energy split (1.5 eV) between T_2 and T_1 and the small energy split (0.09 eV) between T_2 and S_1 verified the origin of the special energy levels of TPATCN in the excited state.

2.3. Photophysical Properties

The solution and solid-state UV–vis absorption and photoluminescence emission spectra of TPATCN are shown in **Figure 2** and the relevant data are summarized in **Table 1**. The absorption spectrum in solution exhibited a low-energy intramolecular CT transition with absorption maximum at 445 nm. The CT character of the excited state was further evidenced

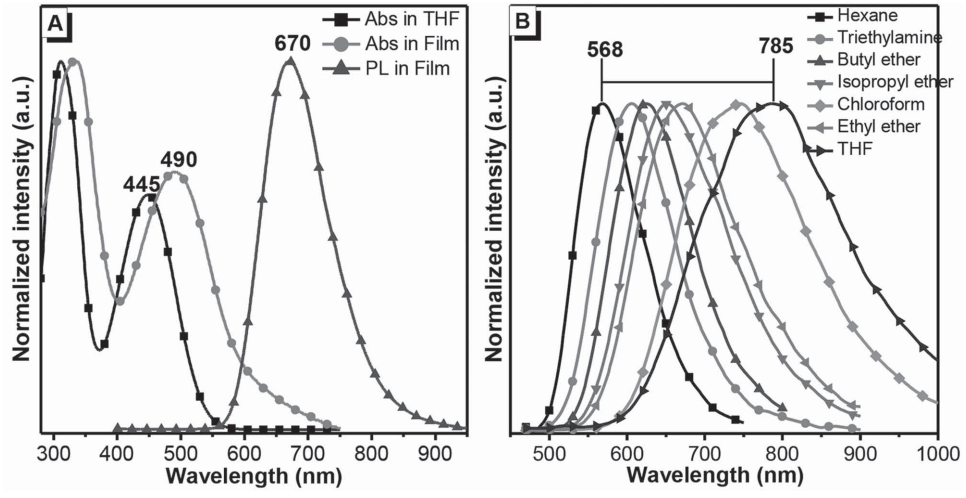

Figure 2. A) The UV–vis spectra in diluted THF solution (concentration: 1×10^{-5} mol L^{-1}), the UV–vis and PL spectra in vacuum-evaporated film (excitation wavelength (λ_{ex}): 490 nm); B) solvatochromic PL spectra with increasing polarity of solvents (λ_{ex}: 445 nm).

Table 1. Detailed photophysical data of TPATCN in different solvents.

Solvent	Δf	λ_{abs} [a] [nm]	λ_{em} [b] [nm]	Stokes shift [cm^{-1}]	Φ_F [c] [%]
Hexane	0	449	564	4541	94.9
Cyclohexane	0	451	572	4690	89.2
p-Xylene	0.003	466	620	5330	74.8
CCl_4	0.011	465	596	4727	86.0
Toluene	0.014	463	628	5674	74.9
Butyl ether	0.096	456	622	5852	91.7
Isopropyl ether	0.145	451	650	6788	62.2
Ether	0.167	448	660	7170	64.9
Chloroform	0.149	469	722	7471	26.1
Ethyl acetate	0.200	440	740	9217	1.8
Tetrahydrofuran	0.210	446	790	9763	3.4
Dichloromethane	0.218	460	806	9332	1.6
Acetone	0.284	440	–[d]	–	–

[a]Absorption maximum; [b]Emission maximum; [c]Fluorescence quantum yield estimated by using Rhodamine B as standard (Φ_F = 70% in ethanol); [d]Not detectable (signal too weak to be accurately determined).

by the redshift of the emission maximum upon increasing solvent polarity. For instance, the emission peak shifted from green emission peaking at 568 nm to NIR emission peaking at 785 nm when measured in nonpolar hexane and moderate polar THF, respectively. Correspondingly, the photoluminescent quantum yields were continuously decreased from 95% to ≈1.6% when the solvent was varied from hexane to dichloromethane. This is a common photophysical phenomenon arised from intramolecular CT,[5,9] which is featured with emission redshift and emission intensity decreasing with increasing solvent polarity.

To better understand the excited state properties, the Stokes shift ($\nu_a - \nu_f$) versus the orientation polarizability $f(\varepsilon,n)$ was fitted for TPATCN according to the Lippert–Mataga relation.[16] As shown in **Figure 3**, TPATCN displayed two-section linear relations with μ_e of 16.7 and 32.9 D in low- and high-polarity solvents, respectively, corresponding to the LE and CT states. In low-polarity solvents, the μ_e of 16.7 D and the maintenance of relatively high photoluminescence quantum yields (η_{PL}) indicated the coexistence of CT and LE characteristics of S_1 state. In contrast, the η_{PL} of TPATCN drastically decreased in high-polarity solvents, which was only 1.6% in dichloromethane. Simultaneously, the μ_e of 32.9 D was much larger than that of 23 D for 4-(*N*,*N*′-dimethylamino)-benzonitrile (DMABN, a typical CT state molecule).[17] Therefore, it could be concluded that a CT state was dominant in high-polarity solvents. Furthermore, time-resolved experiment revealed a monoexponential decay of S_1 state in low polarity solvents (**Figure 4**; Figure S11 and Table S2, Supporting Information) implying that LE and CT components of TPATCN were combined into HLCT state, which was consistent with theoretical calculation results as discussed above.

We also investigated the PL of TPATCN in THF/water mixtures. As shown in **Figure 5**, the THF solution of TPATCN-emitted NIR fluorescence peaking at 770 nm. When the water content (f_w) was increased from 0 to 50%, the emission intensity of TPATCN was weakened and the emission maximum had an apparent redshift. The origin of weak fluorescence in pure THF was related to the twisted configuration and the corresponding intramolecular motions, which induced the CT effects and led to the relatively low efficiency in THF. When f_w continued to increase from 60% to 90%, the emission peak maximum appeared an unusual blueshift and the intensity was increased quickly, indicating that the molecules aggregation began to occur and enhanced by further increase in the water fraction. The fluorescence spectra were affected less by the solvent polarity and the emission profile in the aggregated state was blueshifted. The emission peak of its thin film was further blue-shifted from those in aqueous mixture because of com-

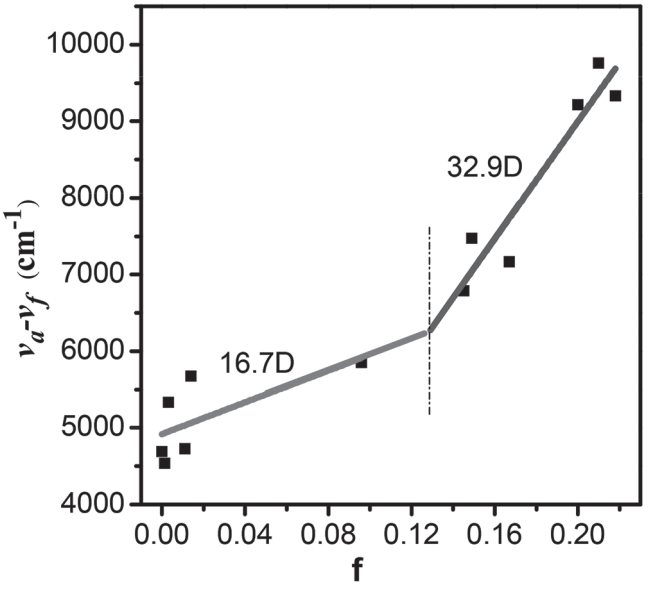

Figure 3. Linear fitting of Lippert–Mataga model (*f*: orientation polarization of solvent media; $\nu_a - \nu_f$: Stokes shift of TPATCN in different solvent).

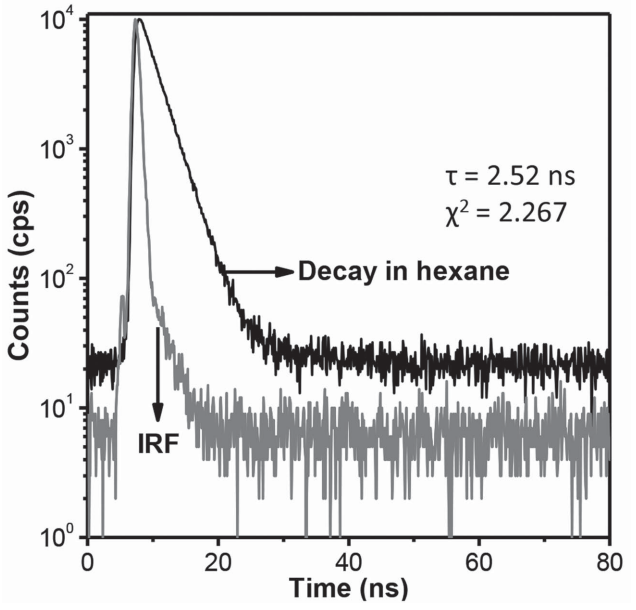

Figure 4. Lifetime measurement of TPATCN in nonpolar hexane solvent.

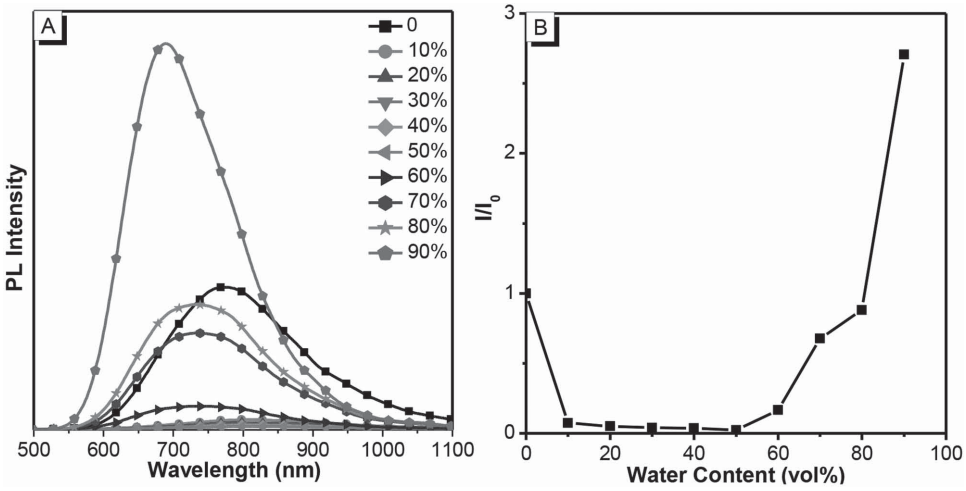

Figure 5. A) PL spectra of TPATCN (10 μm) in THF/water mixtures with different water fractions; B) relations between the ratio of I/I_0 and water fraction in H_2O/THF mixtures; I_0 and I were the maximum PL intensity of TPATCN in pure THF and in H_2O/THF mixtures (10×10^{-6} M), respectively.

plete elimination of the solvent polarity effect.[18] The nature of aggregation enhanced emission characteristics of TPATCN should be associated with a more efficient radiative electron transition in aggregated state than the CT state in polar solvents.

In thin film, TPATCN showed an absorption band at 490 nm and the bandgap was calculated to be 1.97 eV according to the onset of the absorption spectrum. The emission peak of film was at 670 nm, and the Stokes shift was measured to be 5482 cm^{-1}, corresponding to HLCT characteristics in the region of low-polarity solvents (5330 cm^{-1} in *p*-xylene). The emission maximum of solid powder located at 622 nm (Figure 7), which was blue-shifted from the thin film suggesting the different molecular packing mode in solid states. The fluorescence quantum efficiencies (Φ_F) of TPATCN film and powder reached 33% and 42% measured by integrating sphere system, respectively. These values are pretty high for D–A-type NIR emitters reported so far, which proves that our design strategy is reasonable.

2.4. Crystal Structure

The red needle-like crystal is obtained by slow diffusion of methylene dichloride into ethanol solution. The collected crystal is good enough for single crystal X-ray diffraction analysis, and the data are summarized in Table S1 (Supporting Information). The crystal structure belonged to triclinic crystal system with space group of *P*-1 and there were two molecules in one unit cell. As shown in **Figure 6**, TPATCN displayed a

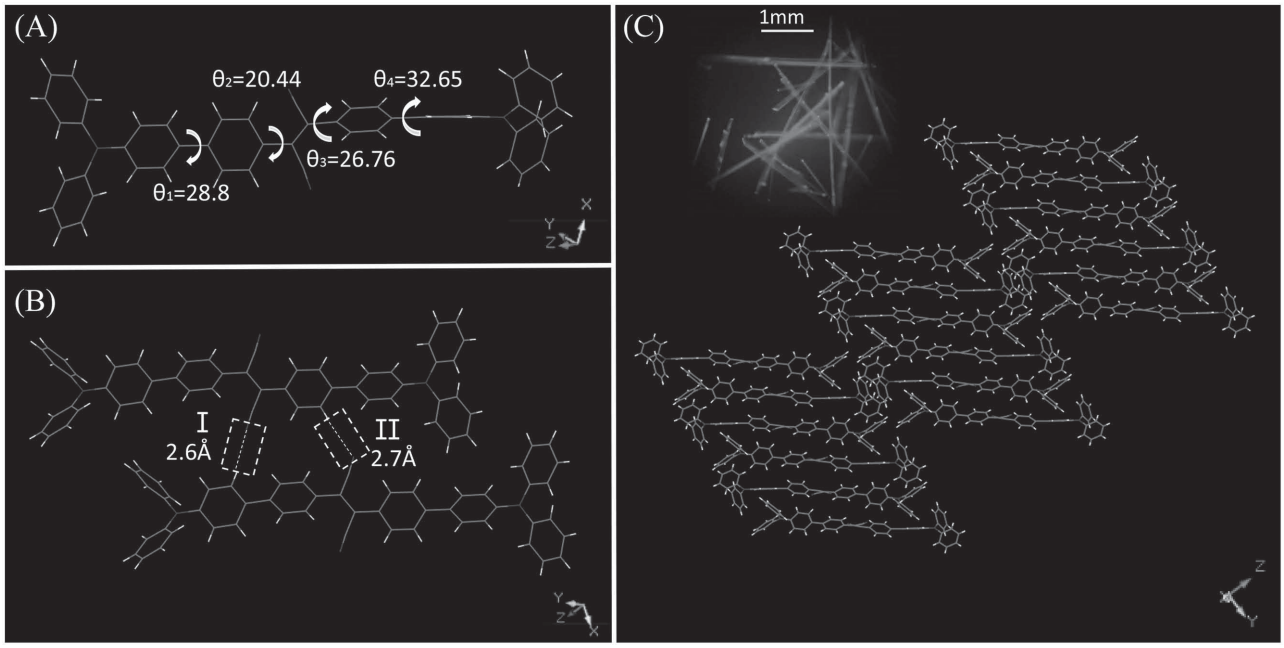

Figure 6. A) Molecular configuration of TPATCN; B) the C—H···N hydrogen bond between adjacent molecules; C) crystal packing and the photo of crystal under the microscope.

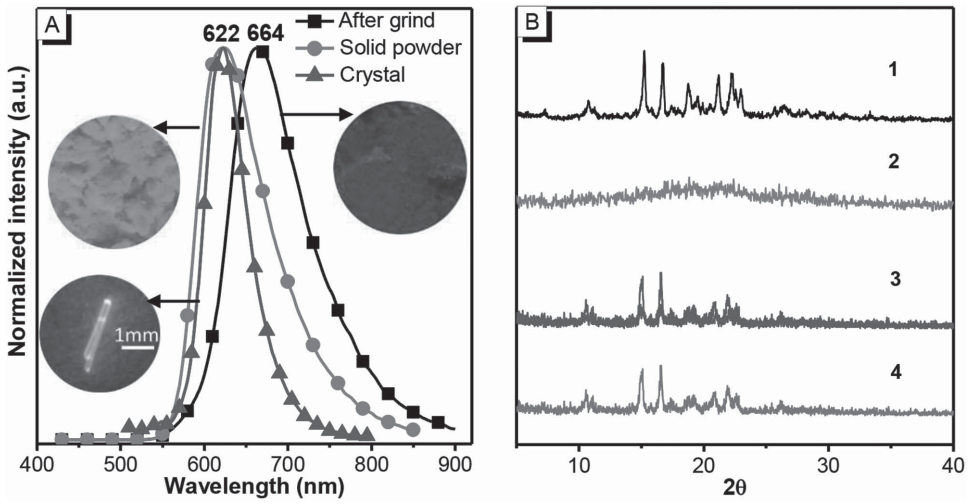

Figure 7. A) The PL spectra and photos of TPATCN powder before and after grinding. B) XRD patterns of TPATCN solids (1) as-prepared powder; (2) ground powder; (3) after thermal annealing; (4) fumed with DCM (λ_{ex}: 490 nm).

highly twisted molecular conformation. The dihedral angles between the TPA substituents and the central phenyl ring were as big as 28.8° (θ_1) and 32.65° (θ_4), respectively. The dihedral angles between fumaronitrile core and two phenyl rings were 20.44° (θ_2) and 26.76° (θ_3), respectively. There were two kinds of C—H···N hydrogen bonds between the adjacent molecules. Hydrogen bond I was formed between cyano group and hydrogen atom on the TPA group of the adjacent molecule with a distance of 2.6 Å. Hydrogen bond was formed between the other cyano group and hydrogen atom on the phenyl ring of the neighboring molecule with a distance of 2.7 Å. As can be seen from **Figure 7**, the emission peak of TPATCN crystal was located at 622 nm which was very similar to the solid powder. However, the full width at half maximum (FWHM) of the emission spectra was only 60 nm, which was nearly 40 nm less than the corresponding emission in solid powder. In the crystal, TPATCN was highly orderly arranged and the multiple hydrogen bonds could help to rigidify the molecular conformation and lock the molecular rotations, which reduced the possible energy loss through the nonradiative rotational relaxation channel and endowed the crystal with a very high efficiency. In particular, the crystal possessed an intense emission with a high quantum efficiency up to 72%.

2.5. Piezochromic Property

The emission color of TPATCN powder can be changed easily by external stimuli, which gives rise to the significant change in physicochemical and photochemical properties. For example (Figure 7), the powder of TPATCN exhibited a strong red emission under illumination of a 365 nm UV light. Upon grinding, the wavelength of PL spectrum was redshifted displaying NIR emission. And after annealing the ground sample at 150 °C for 5 min or solvent fumigation (such as DCM or THF), the initial color and emission could be restored. To determine the mechanism of the piezofluorochromic effect, wide-angle X-ray diffraction (WXRD) measurements were carried out for each sample. It was found that the powder of TPATCN displayed intense and sharp diffraction peaks indicating its crystalline state of the solid. After grinding, the XRD profile gave no noticeable diffraction, reflecting its amorphous feature in this state. After fuming or annealing, the WXRD curve diffraction peaks were recovered to reform the crystalline structure. Further inspection of the differential scanning calorimetry (DSC) curve (Figure S5, Supporting Information) of the grind powder revealed cold-crystallization transition peaks at 105 and 125 °C prior to melting at 246 °C in the first heating scan, which was absent in the thermograms of both annealed and fumed samples. The results indicated that the TPATCN was presented in a metastable amorphous phase and converted to a stable crystalline phase via an exothermal recrystallization process. The results were consistent with the WXRD experimental data demonstrating that the mechanochromism phenomenon was resulted from the transformation between the crystalline and amorphous states.[17]

2.6. Electroluminescence

The high PL efficiency of TPATCN in the solid state promotes its application in OLEDs performance. A non-doped NIR OLEDs with the configuration of ITO/PEDOT:PSS(40 nm)/NPB(40 nm)/EML(20 nm)/BCP(10 nm)/AlQ_3(50 nm)/LiF(0.5 nm)/Al(120 nm) was fabricated. (ITO: indium-tin oxide; PEDOT:PSS: poly(3,4-ethylenedioxythiophene:poly(styrenesulfonate); NPB: *N,N′*-bis(1-naphthyl)-*N,N′*-biphenyl-1,1′-biphenyl-4,4′-diamine); EML: emitting material layer; BCP: bathocuproine; AlQ3: tris-(8-hydroxyquinolinato)aluminum.) TPATCN exhibited NIR EL peaking at 675 nm with a Commission Internationale de L'Eclairage (CIE) coordinate of (0.673, 0.324), which was almost identical to the PL spectrum of the evaporated film. The turn-on voltage of the device was relatively low as 3.6 V, which benefited from the decreased injection barriers regulated by the D–A moieties. The maximum luminance was as high as 7025 cd m^{-2}, and the EQE could reach 2.58%, which is among the best performance of NIR OLEDs. Unlike many

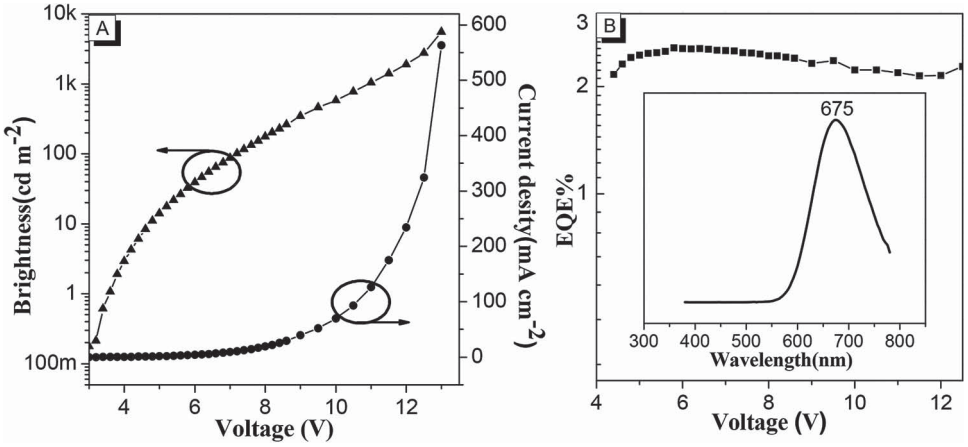

Figure 8. A) Luminance and current density at different driving voltage; B) EQE-voltage characteristics of nondoped device. Inset: EL spectrum at 5 V.

phosphorescent materials based NIR OLEDs which usually showed sharp efficiency roll-off at high brightness,[3] the EQE of the non-doped TPATCN device was kept almost unchanged even at a high current density of 200 mA cm^{-2}, suggesting the very low roll-off of external efficiency (**Figure 8**, **Table 2**). Equation (1) is applied to calculate the theoretical value of the radiative excition ratio. Assuming the light outcoupling efficiency of 20% and the 100% hole–electron recombination in the OLED, the theoretical value of the radiative exciton ratio was calculated to be 39%, which breaked through the spin statistics limit of 25% (singlet/triplet ratio 1/3). Such high EL performances are impressive and outperform the previous literature results.[11,19] No delayed fluorescence was observed from transient PL and the device had no luminance efficiency roll-off with current density increasing, which is in accordance with our demonstration of HLCT mechanism.

3. Conclusion

In summary, a NIR light-emitting D–A compound, TPATCN, is rationally designed and synthesized using TPA as the donor and DBFN as the acceptor. TPATCN shows AIE behavior in aggregated state, stimuli-responsive property, and strong NIR emission ($\lambda_{em,film}$ = 670 nm, $\Phi_{F,film}$ = 33%, $\Phi_{F,crystal}$ = 72%). Photophysical and DFT analysis reveals that TPATCN possesses the large dipole moment of the CT state and a certain degree of orbital of the LE state originating from the newly discovered excited-state characteristics of the DFCN, endowing TPATCN a potentially highly efficient material. In EL performance, the maximum EQE of nondoped device reaches 2.58% with a maximum luminance of 7025 cd m^{-2}, which is among the highest values observed for nondoped NIR OLEDs. Remarkably, the EQE of the device remains fairly constant over a range of 100–300 mA cm^{-2}. A high radiative exciton ratio of 39% is observed, which exceeds the limit of 25% in conventional OLEDs, probably as a result of efficient RISC through the "hot-exciton" process. Our study should provide new ideas for the design of efficient NIR-fluorescent molecules by emphasizing the full use of both singlet and triplet excitons.

Table 2. EL performance of nondoped devices using TPATCN as emitter.

Device	λ_{max} [a] [nm]	$V_{turn\text{-}on}$ [b] [V]	L_{max} [c] [cd m^{-2}]	LE_{max} [d] [cd A^{-1}]	PE_{max} [e] [lm W^{-1}]	EQE_{max} [f] [%]
TPATCN	675	3.6	7025	0.96	0.59	2.58

[a]Maximum peak of EL spectra; [b]Turn-on voltage recorded at the luminance of 1 cd m^{-2}; [c]Maximum luminance; [d]Maximum luminous efficiency; [e]Maximum power efficiency; [f]Maximum external quantum efficiency.

4. Experimental Section

Materials: All the reagents and solvents used for the synthesis and characterization were purchased from Aldrich and Acros and used as received.

Synthesis of 2,3-bis(4-Bromophenyl)Fumaronitrile (M2): M1 (5.1 mmol) and I_2 (5.1 mmol) were dissolved in diethyl ether under nitrogen. The system temperature was stabilized at −78 °C, and sodium methylate (10.71 mmol) was added to the reaction system and stirred for 30 min. Then, the reaction mixture was transferred to ice water and stirred for further 4 h. Thereafter, a small amount of 3% HCl(aq) was added to complete the reaction, and then M2 was isolated by simple suction filtration of the reaction solution (yield 70%).

Synthesis of 2,3-bis(4′-(Diphenylamino)-[1,1′-Biphenyl]-4-yl)Fumaronitrile (TPATCN): A mixture of M2 (2.0 mmol), M3 (4.4 mmol), sodium carbonate (20 mmol), toluene (30 mL), absolute alcohol (8 mL), and $Pd(PPh_3)_4$ (100 mg) was refluxed at 90 °C for 48 h under nitrogen. After the mixture was cooled down, 40 mL water was added to the resulting solution and the mixture was extracted with CH_2Cl_2 for three times. The organic phase was dried over Na_2SO_4. After filtration and solvent evaporation, the liquid was purified by chromatography using the mixture of CH_2Cl_2/petroleum ether as the eluent to afford a red solid (yield 58%). ^{1}H NMR (500 MHz, $CDCl_3$, δ): 7.94–7.91 (m, 4H), 7.73 (d, J = 8.5 Hz, 4H), 7.55–7.51 (m, 4H), 7.32–7.27 (m, 8H), 7.16 (dd, J = 8.2, 2.0 Hz, 12H), 7.07 (t, J = 7.4 Hz, 4H). MS (ESI) m/z: $[M]^+$ calcd for $C_{52}H_{36}N_4$, 717.3; found, 717.8. Anal. calcd for $C_{52}H_{36}N_4$: C 87.12, H 5.06, N 7.82; found: C 87.10, H 5.06, N 7.84.

General Details: The ^{1}H NMR data were recorded on a Bruker AVANCE 500 spectrometer at 500 MHz using tetramethylsilane (TMS) as the internal standard and $CDCl_3$ as solvent. Elemental analysis was performed on a Flash EA 1112, CHNS-O elemental analysis instrument. The high-resolution mass spectrum was measured using an Agilent1290-micrOTOF Q II instrument. Thermal gravimetric analysis (TGA) was measured on a Perkin-Elmer thermal analysis system from 30 to 800 °C at a heating rate of 10 K min^{-1} under nitrogen

flow rate of 80 mL min^{-1}. DSC was performed on a NETZSCH (DSC-204) unit from 0 to 300 °C at a heating rate of 10 K min^{-1} under nitrogen atmosphere. The electrochemical properties (oxidation and reduction potentials) were carried out via cyclic voltammetry (CV) measurements by using a standard one-compartment, three-electrode electrochemical cell given by a BAS 100B/W electrochemical analyzer. 0.1 M tetrabutylammoniumhexafluorophosphate ($TBAPF_6$) in anhydrous dimethyl formamide (DMF) or anhydrous dichloromethane was used as the electrolyte for negative or positive scan. A glass–carbon disk electrode was used as the working electrode, a Pt wire as the counter electrode, and Ag/Ag^+ as the reference electrode together with ferrocene as the internal standard at a scan rate of 100 mV s^{-1}. UV–vis and fluorescence spectra were recorded on a Shimadzu UV-3100 spectrophotometer using 1 cm path length quartz cells. The fluorescence lifetime and quantum efficiency of solid film were carried out with FLS920 Spectrometer. The Φ_F of different solutions were measured by using Rhodamine B as a reference (Φ_F = 0.7 in ethanol) and were calculated by using the following formula

$$Q_X = Q_r \left(\frac{A_r(\lambda_r)}{A_X(\lambda_X)}\right)\left(\frac{I(\lambda_r)}{I(\lambda_X)}\right)\left(\frac{n_X^2}{n_r^2}\right)\left(\frac{D_X}{D_r}\right) \quad (2)$$

where Q is the quantum efficiency, A is the value of absorbance, I is the intensity of excitation source, n is the refractive index of solvent, D is the area of emission spectra, and λ is the corresponding wavelength. The subscript r stands for the reference and X stands for test subject. The excitation wavelengths were their absorption maxima.

Device Fabrication: ITO-coated glass was used as the substrate and the sheet resistance was 15 Ω $square^{-1}$. The ITO glass substrates were cleaned with isopropyl alcohol, acetone, toluene, and deionized water, dried in an oven at 120 °C, treated with UV-zone for 20 min, and finally transferred to a vacuum deposition system with a base pressure lower than 5×10^{-6} mbar for organic and metal deposition. The hole injecting PEDOT layer (40 nm). The deposition rate of all organic layers was 0.3 Å s^{-1}. The electron injection LiF layer (1 nm) was deposited at a rate of 0.1 Å s^{-1} and then the capping Al metal layer (100 nm) was deposited at a rate of 5.0 Å s^{-1}. The EL characteristics were measured using a Keithley 2400 programmable electrometer and a PR-650 Spectroscan spectrometer under ambient condition at room temperature.

Computational Details: The ground state (S_0) and the lowest singlet excited state (S_1) geometries were optimized at the B3LYP/6-31G(d,p) level, which is a common method to provide molecular geometries and the optimized outcome is in good agreement with the experiment result. The energy levels of both singlet and triplet states were calculated using TD-M062X/6-31G(d,p) method on the basis of the optimized configuration of S_0 and S_1, respectively. For the purpose of investigating the properties of excited states, NTOs of absorption were evaluated for ten lowest excited states, involving both singlet and triplet states under TD-M062X/6-31G(d,p) level. This approach provides the most compact representation of the electronic transitions in terms of an expansion into single particle orbitals by diagonalizing the transition density matrix associated with each excitation. All the calculations were carried out using Gaussian 09 (version D.01) package.

Single Crystal Measurements: The single crystal of TPATCN was performed on a Rigaku R-AXIS RAPID diffractometer equipped with a graphite monochromated Mo Kα radiation source. The diffraction data were collected at room temperatures. The structure was determined using direct methods with the SHELXL-97 software program. X-ray diffraction of powder was carried out with a Rigaku Smart Lab (3) diffractometer. The sample placed on a glass plate (glass thickness: 0.05 mm) was irradiated by Cu Kα radiation source (voltage: 40 kV; current: 30 mA).

Lippert–Mataga Calculation: The properties of ground state (S_0) and the lowest singlet excited state (S_1) can be better understood through solvatochromic experiment. One reliable way to explore the influence of solvent environment on the optical property of our sample is by using the Lippert–Mataga equation, a model that describes the interactions between the solvent and the dipole moment of solute

$$hc(\nu_a - \nu_f) = hc(\nu_a^0 - \nu_f^0) - \frac{2(\mu_e - \mu_g)^2}{a^3} f(\varepsilon,n) \quad (3)$$

where f is the orientational polarizability of the solvent; $\nu_a^0 - \nu_f^0$ corresponds to the Stokes shifts when f is zero; μ_e is the excited state dipole moment; μ_g is the ground-state dipole moment; a is the solvent cavity (Onsager) radius, derived from the Avogadro number (N), molecular weight (M), and density (d = 1.0 g cm^{-3}); ε and n are the solvent dielectric and the solvent refractive index, respectively; $f(\varepsilon,n)$ and a can be calculated respectively as follows

$$f(\varepsilon,n) = \frac{\varepsilon - 1}{2\varepsilon + 1} - \frac{n^2 - 1}{2n^2 + 1} \quad (4)$$

CCDC 1414550 contains the supplementary crystallographic data for this paper. These data can be obtained free of charge from the Cambridge Crystallographic Data Centre via www.ccdc.cam.ac.uk/data_request/cif.

Supporting Information

Supporting Information is available from the Wiley Online Library or from the author.

Acknowledgements

This work was supported by the Ministry of Science and Technology of China (Grant No. 2013CB834801), the National Science Foundation of China (Grant Nos. 21374038 and 91233113), and the Graduate Innovation Fund of Jilin University (Project 2014011).

Received: August 10, 2015
Revised: September 27, 2015
Published online: November 10, 2015

[1] a) A. C. Grimsdale, K. L. Chan, R. E. Martin, P. G. Jokisz, A B. Holmes, *Chem. Rev.* **2009**, *109*, 897; b) H. Xu, R. F. Chen, Q. Sun, W. Y. Lai, Q. Q. Su, W. Huang, X. G. Liu, *Chem. Soc. Rev.* **2014**, *43*, 3259; c) X. F. Ren, J. Li, R. J. Holmes, P. I. Djurovich, S. R. Forrest, M. E. Thompson, *Chem. Mater.* **2004**, *16*, 4743; d) H. Uoyama, K. Goushi, K. Shizu, H. Nomura, C. Adachi, *Nature* **2012**, *492*, 234; e) Q. S. Zhang, J. Li, K. Shizu, S. Huang, S. Hirata, H. Miyazaki, C. Adachi, *J. Am. Chem. Soc.* **2012**, *134*, 14706; f) L. X. Xiao, X. Xing, Z. J. Chen, B. Qu, H. L. Lan, Q. H. Gong, J. Kido, *Adv. Funct. Mater.* **2013**, *23*, 1323; g) Y. J. Cho, S. K. Jeon, B. D. Chin, E. Yu, J. Y. Lee, *Angew. Chem. Int. Ed.* **2015**, *54*, 5201.

[2] a) J. Huang, Q. Liu, X. H. Zhu, X. H. Zhu, A. Y. Li, J. W. Li, S. Wu, J. B. Peng, Y. Cao, R. D. Xia, D. D. C. Bradley, J. Roncali, *Adv. Funct. Mater.* **2009**, *19*, 2978; b) W. Qin, D. Ding, J. Z. Liu, W. Z. Yuan, Y. Hu, B. Liu, B. Z. Tang, *Adv. Funct. Mater.* **2012**, *22*, 771; c) B. Stender, S. F. Volker, *Adv. Mater.* **2013**, *25*, 2943; d) B. N. G. Giepmans, S. R. Adams, M. H. Ellisman, R. Y. Tsien, *Science* **2006**, *312*, 217.

[3] K. R. Graham, Y. X. Yang, J. R. Sommer, A. H. Shelton, K. S. Schanze, J. X. Xue, J. R. Reynolds, *Chem. Mater.* **2011**, *23*, 5305.

[4] a) T. J. Weil, T. Vosch, J. Hofkens, K. Peneva, K. Müllen, *Angew. Chem. Int. Ed.* **2010**, *49*, 9068; b) X. W. Zhan, A. Facchetti, S. Barlow, T. J. Marks, M. A. Ratner, M. R. Wasielewski, S. R. Marder, *Adv. Mater.* **2011**, *23*, 268; c) Y. Yamaguchi, Y. Matsubara, T. Ochi, T. Wakamiya, Z. Yoshida, *J. Am. Chem. Soc.* **2008**, *130*, 13867.

[5] a) X. B. Du, J. Qi, Z. Q. Zhang, D. G. Ma, Z. Y. Wang, *Chem. Mater.* **2012**, *24*, 2178; b) S. Ellinger, K. R. Graham, P. J. Shi, R. T. Farley, T. T. Steckler, R. N. Brookins, P. Taranekar, J. G. Mei, L. A. Padilha, T. R. Ensley, H. H. Hu, S. Webster, D. J. Hagan, E. W. Van Stryland, K. S. Schanze, J. R. Reynolds, *Chem. Mater.* **2011**, *23*, 3805.

[6] a) C. L. Chiang, M. F. Wu, D. C. Dai, Y. S. Wen, J. K. Wang, C. T. Chen, *Adv. Funct. Mater.* **2005**, *15*, 231; b) G. Qian, Z. Zhong, M. Luo, D. Yu, Z. Zhang, D. Ma, Z. Y. Wang, *J. Phys. Chem. C* **2009**, *113*, 1589.

[7] a) J. V. Caspar, E. M. Kober, B. P. Sullivan, T. J. Meyer, *J. Am. Chem. Soc.* **1982**, *104*, 630; b) S. D. Cummings, R. Eisenberg, *J. Am. Chem. Soc.* **1996**, *118*, 1949; c) M. V. Auwraer, Z. R. Grabowski, *J. Phys. Chem.* **1991**, *95*, 2083; d) M. Shimizu, R. Kaki, *Angew. Chem. Int. Ed.* **2012**, *51*, 4095.

[8] a) S. Reineke, M. A. Baldo, *Phys. Status Solidi A* **2012**, *209*, 2341; b) S. O. Jeon, S. E. Jang, H. S. Son, J. Y. Lee, *Adv. Mater.* **2011**, *23*, 1436; c) S. J. Su, E. Gonmori, H. H. Sasabe, J. Kido, *Adv. Mater.* **2008**, *20*, 4189; d) Y. Y. Liang, Z. Xu, G. Li, L. P. Yu, *Adv. Mater.* **2010**, *22*, 135.

[9] a) W. J. Li, D. D. Liu, F. Z. Shen, D. G. Ma, Z. M. Wang, T. Feng, Y. X. Xu, B. Yang, Y. G. Ma, *Adv. Funct. Mater.* **2012**, *22*, 2797; b) S. T. Zhang, L. Yao, Q. M. Peng, W. J. Li, Y. Y. Pan, X. Ran, Y. Gao, C. Gu, Z. M. Wang, P. Lu, F. Li, S. J. Su, B. Yang, Y. G. Ma, *Adv. Funct. Mater.* **2015**, *25*, 1755; c) L. Yao, S. T. Zhang, B. Yang, Y. G. Ma, *Angew. Chem. Int. Ed.* **2014**, *53*, 2119; d) W. J. Li, Y. Y. Pan, X. Ran, Q. M. Peng, D. G. Ma, F. Li, F. Z. Shen, Y. H. Wang, B. Yang, Y. G. Ma, *Adv. Funct. Mater.* **2014**, *24*, 1609.

[10] a) G. Qian, B. Dai, D. B. Yu, J. Zhan, Z. Q. Zhang, D. G. Ma, Z. Y. Wang, *Chem. Mater.* **2008**, *20*, 6208; b) C. T. Chen, *Chem. Mater.* **2004**, *16*, 4389; c) Z. H. Li, M. S. Wong, H. Fukutani, Y. Tao, *Chem. Mater.* **2005**, *17*, 5032; d) E. Bundgaard, F. C. Krebs, *Macromolecules* **2006**, *39*, 2823; e) X. Du, J. Qi, Z. Q. Zhang, D. G. Ma, Z. Y. Wang, *Chem. Mater.* **2012**, *24*, 2178; f) S. Kato, T. Matsumoto, M. Shigeiwa, H. Gorohmary, S. Maeda, T. Ishi-i, S. Mataka, *Chem. Eur. J.* **2006**, *12*, 2303.

[11] H. C. Yeh, S. J. Yeh, C. T. Chen, *Chem. Commun.* **2003**, 2632.

[12] X. Y. Shen, Y. J. Wang, E. G. Zhao, W. Z. Yuan, Y. Liu, P. Lu, A. J. Qin, Y. G. Ma, J. Z. Sun, B. Z. Tang, *J. Phys. Chem. C* **2013**, *117*, 7334.

[13] a) S. K. Kim, B. Yang, Y. Park, Y. G. Ma, J. Y. Lee, H. J. Kim, J. W. Park, *Org. Electron.* **2009**, *10*, 822; b) S. Tang, W. J. Li, F. Z. Shen, D. D. Liu, B. Yang, Y. G. Ma, *J. Mater. Chem.* **2012**, *22*, 4401; c) K. Panthi, R. M. Adhikari, T. H. Kinstle, *J. Phys. Chem. A* **2010**, *114*, 4542; d) C. Y. Chan, Z. Zhao, J. W. Y. Lam, J. Z. Liu, S. M. Chen, H. H. Y. Sung, H. S. Kwok, Y. G. Ma, I. D. Williams, K. S. Wong, B. Z. Tang, *Adv. Funct. Mater.* **2012**, *22*, 378.

[14] M. J. Frisch, G. W. Trucks, H. B. Schlegel, G. E. Scuseria, M. A. Robb, J. R. Cheeseman, G. Scalmani, V. Barone, B. Mennucci, G. A. Petersson, H. Nakatsuji, M. Caricato, X. Li, H. P. Hratchian, A. F. Izmaylov, J. Bloino, G. Zheng, J. L. Sonnenberg, M. Hada, M. Ehara, K. Toyota, R. Fukuda, J. Hasegawa, M. Ishida, T. Nakajima, Y. Honda, O. Kitao, H. Nakai, T. Vreven, J. A. Montgomery Jr., J. E. Peralta, F. Ogliaro, M. Bearpark, J. J. Heyd, E. Brothers, K. N. Kudin, V. N. Staroverov, R. Kobayashi, J. Normand, K. Raghavachari, A. Rendell, J. C. Burant, S. S. Iyengar, J. Tomasi, M. Cossi, N. Rega, J. M. Millam, M. Klene, J. E. Knox, J. B. Cross, V. Bakken, C. Adamo, J. Jaramillo, R. Gomperts, R. E. Stratmann, O. Yazyev, A. J. Austin, R. Cammi, C. Pomelli, J. W. Ochterski, R. L. Martin, K. Morokuma, V. G. Zakrzewski, G. A. Voth, P. Salvador, J. J. Dannenberg, S. Dapprich, A. D. Daniels, Ö. Farkas, J. B. Foresman, J. V. Ortiz, J. Cioslowski, D. J. Fox, *Gaussian 09, Revision D.01*, Gaussian, Wallingford, CT **2009**.

[15] S. Difley, D. Beljonne, T. V. Voorhis, *J. Am. Chem. Soc.* **2008**, *130*, 3420.

[16] Z. R. Grabowski, K. Rotkiewicz, *Chem. Rev.* **2003**, *103*, 3899.

[17] a) B. Peng, S. Xu, Z. Chi, J. Xu, *Prog. Chem.* **2013**, *25*, 1805; b) J. R. Xu, Z. G. Chi, *Mechanochromic Fluorescent Materials Phenomena, Materials and Applications*, The Royal Society of Chemistry, London, UK **2014**.

[18] a) D. Xiao, X. Lu, W. Yang, H. Fu, Z. G. Shuai, Y. Fang, J. N. Yao, *J. Am. Chem. Soc.* **2003**, *125*, 6740; b) Y. J. Zhang, J. Sun, G. Bian, Y. Chen, M. Ouyang, B. Hu, C. Zhang, *Photochem. Photobiol. Sci.* **2012**, *11*, 1414.

[19] a) Y. Yang, R. T. Farley, J. Xue, *J. Appl. Phys.* **2009**, *106*, 044509; b) Z. J. Zhao, C. M. Deng, S. M. Chen, J. W. Y. Lam, W. Qin, P. Lu, Z. M. Wang, H. S. Kwok, Y. G. Ma, H. Y. Qiu, B. Z. Tang, *Chem. Commun.* **2011**, *47*, 8847.